Classification:

PHYSICAL SCIENCES: Biophysics and Computational Biology

Title:

Cellular heterogeneity in pressure and growth emerges from tissue topology and geometry

Yuchen Long[1,*], Ibrahim Cheddadi[2,4], Vincent Mirabet[1], Gabriella Mosca[3], Mathilde Dumond[1,5], Jan Traas[1], Christophe Godin[1,2], Arezki Boudaoud[1,*].

1. Laboratoire Reproduction et Développement des Plantes, Université de Lyon, ENS de Lyon, UCB Lyon 1, CNRS, INRA, INRIA, F-69342, Lyon, France.

2. INRIA/CIRAD/INRA Project-team Virtual Plants, France.

3. Department of Plant and Microbial Biology, University of Zürich, Zollikerstrasse 107, CH-8008 Zürich, Switzerland.

4. Current address: Univ. Grenoble Alpes, CNRS, Grenoble INP, TIMC-IMAG, 38000 Grenoble, France.

5. Current address: Department of Biosystems Science and Engineering, ETH Zurich, Mattenstrasse 26, 4058, Basel, Switzerland.

*. Correspondence and requests for materials should be addressed to yuchen.long@ens-lyon.fr or arezki.boudaoud@ens-lyon.fr

The authors declare no competing financial interests.

Abstract

Cell-to-cell heterogeneity prevails in many biological systems, although its origin and function are often unclear. Cell hydrostatic pressure, alias turgor pressure, is an essential property in tissue physiology and morphogenesis, and its spatial variations are often overlooked. Here, using micro-indentation by atomic force microscope, we find that hydrostatic pressure is heterogeneous between adjacent cells in the epidermis of Arabidopsis shoot apical meristem, a population of stem cells from which originate all aerial organs of the plant. Combining experiments and physical modelling of cell wall mechanics and water movement, we propose that cell size and tissue topology contribute to the patterning of heterogeneities in pressure and growth, partially reminiscent of a liquid foam. Pressure correlates either positively or negatively with cellular growth rate depending on conditions, suggesting that the meristem is at a tipping point between limitation of growth by cell wall extensibility and by water conductivity. Together, our results shed light on spatial variations of pressure and growth rate, with potential roles in tissue homeostasis.

Key words

Cellular heterogeneity, hydrostatic pressure, tissue topology, growth mechanics, tissue hydraulics, atomic force microscopy, biophysical modelling.

Significance statement

Within a living tissue or an organ, cells grow at markedly different rates. Nevertheless, the causes and consequences of such heterogeneity in growth are poorly understood. We therefore examined cell internal pressure and cell growth in a population of stem cells in the model plant Arabidopsis, by combining optical microscopy and biophysical measurements. We found that pressure and growth in a given cell were both correlated with the number of its neighbours, i.e. with local topology. We retrieved experimental observations by using a mathematical model accounting for force propagation and water movement in the tissue. Our work suggests that water availability may be partially limiting for growth and puts forward topology as a source of spatial variations in cell growth.

Introduction

Cell-to-cell fluctuations are observed in many biological phenomena like gene expression, signalling, cell size regulation and growth (1–8). Notably, heterogeneity in cell size and growth rate often prevails and impacts tissue patterning and macroscopic growth robustness (1, 2). Cell volume change is driven by osmosis (9–11) and the resulting intracellular hydrostatic pressure, and is restrained by peripheral constraints (plasma membrane, cytoskeletal cortex, extracellular matrix, or cell wall) in plant (12), animal (13), tumorous (14) and microbial cells (15). Despite numerous studies (15–17), the spatial variation of hydrostatic pressure in multicellular tissues, and its relation with cell-to-cell growth variability, remain elusive.

Due to high difference between internal and external osmotic potential, cells with rigid cell walls – like in plants, bacteria and fungi – accumulate hydrostatic pressure, alias turgor pressure, often greater than atmospheric pressure (Fig. S1) (12). Animal cells also accumulate hydrostatic pressure, especially when compacted or contracting (13, 14), though to a lesser extent than walled cells. In plants, turgor pressure is believed to positively correlate with growth rate, as depicted in the Lockhart-Ortega equation (Fig. S1) (17). However, observations suggest that growth rate and pressure level are not always associated (16), making it difficult to assess and understand the link between growth regulation and cellular pressure build-up. Here, we aimed at addressing this issue in a model plant tissue. We quantified turgor pressure and growth rate in a multicellular tissue and we use a physical model coupling tissue growth mechanics with water movement to account for our observations.

Results

Atomic force microscopy reveals turgor pressure heterogeneity in Arabidopsis shoot apical meristem

Recent advances in atomic force microscopy (AFM) enabled non-invasive turgor pressure retrieval utilizing indentation force-displacement and surface topography in living plant cells (Fig. 1A) (18). Accordingly, we used a pressurized thin-shell model to deduce the turgor pressure value from the AFM-measured force-displacement curve, which is influenced by turgor pressure, cell wall mechanical properties, and cell 3D geometry (Fig. S2; see

77 Supplementary Discussion) (19). We carefully evaluated the contributions of these parameters
78 to the indentation results, and excluded many possible biases in deducing turgor from our AFM
79 approaches (Fig. S2; see Supplementary Discussion). Additionally, influence of tissue context
80 on indentation readout (20) was rigorously tested and ruled out by numerical simulations of
81 indentations on realistic 3D meshes accounting for pressurized epidermal cells (Fig. S8; see
82 Supplementary Discussion). Taken together, we concluded that our AFM measurements are
83 sensitive to cell-to-cell turgor pressure variation, and semi-quantitative in regards to the
84 absolute value of pressure. Accordingly, in the following, we use 'turgor pressure' to qualify
85 the AFM-determined values.

86 We applied AFM-based pressure deduction to the epidermis of the *Arabidopsis thaliana* shoot
87 apical meristem (SAM), a system featuring substantial growth heterogeneity (1). We included
88 untreated wild-type SAMs and a conceptually simpler model of chemically treated SAM that
89 resembles a "foam of cells" (co-treated with naphthylphthalamic acid (NPA), a polar auxin
90 transport inhibitor that induces pin-formed SAMs, and oryzalin, a microtubule-depolymerizing
91 drug that blocks cell division but permits continuous, isotropic growth; hereafter referred to as
92 "oryzalin-treated SAMs") (21). Walls between cells are often curved in growing oryzalin-
93 treated SAMs, like liquid films in a foam, suggesting that neighbouring cells have different
94 turgor pressure (21) in a growing tissue (Fig. S3). Cell-specific AFM measurements on nine
95 SAMs revealed that turgor pressure is markedly heterogeneous in oryzalin-treated SAMs
96 epidermis (Fig. 1E and Fig. S2). Oryzalin-treated SAMs had average turgor pressures spanning
97 the range 0.65 to 1.72 MPa (1.21 ± 0.34 MPa, mean ± standard error of mean; Fig. S4). These
98 values are comparable to the 2.0 MPa osmotic pressure estimated by incipient plasmolysis (Fig.
99 S5). The AFM-determined turgor also decreased with increasing osmolarity of external medium
100 (Fig. S5), further supporting this AFM-based approach.

101 Cell-specific measurements revealed that cellular pressure anticorrelates with the number of
102 epidermal cell-neighbours: cells with fewer neighbours have higher turgor pressure (Fig. S6).
103 We focused on cell-to-cell variations of turgor and we removed variations between SAMs by
104 normalizing cellular pressure to the average pressure per SAM; normalized pressure decreases
105 with neighbour number, being 1.3-fold greater in four- than in eight-neighboured cells (n = 202

cells, Pearson correlation coefficient R = -0.31, $p < 10^{-5}$) (Fig. 1F), consistent with previous prediction (21).

Untreated SAMs exhibit more constant turgor, as determined by AFM, at 2.62 ± 0.03 MPa (Fig. S4), with the same magnitude as the estimated osmotic pressure at 1.2 MPa (Fig. S5) and the preliminary values obtained previously (22) (see Supplementary Discussion). Consistently, we also detected similar, though slightly weaker, turgor–neighbour-number anticorrelation in untreated SAMs (7 SAMs, n = 503 cells, R = -0.16, $p = 10^{-4}$) (Fig. 1G-J and Fig. S6, S7), confirming that non-random turgor pressure heterogeneity establish in tissues with static topology (no neighbour number change) or dynamic topology (neighbour numbers change due to division).

A mechanical-hydraulic model predicts that pressure heterogeneity emerges from tissue topology

Earlier tissue models (21, 23) treated intracellular pressure as an input or required differential osmotic pressure. Nevertheless, the anticorrelation that we find between pressure and neighbour number is reminiscent of liquid foams (24). We therefore tested whether pressure heterogeneity could emerge from the classical plant water relations and wall mechanics (25) (Fig. 2A). We use a 2D vertex model, with topological distribution similar to SAM (Fig. S9), that actually expands the Lockhart-Ortega equation of visco-elasto-plastic growth of single cell (Fig. S1) (17) to cell walls in a multicellular tissue with more realistic 2D polygonal geometry. Each cell wall has a thickness w and behaves as an elastic material of modulus E when wall tension induced by turgor pressure P is low enough, more specifically when the elastic strain (ε, reversible deformation) is lower than a threshold ε^Y. When tension in the wall exceeds the corresponding threshold ($E\varepsilon^Y$), the cell wall undergoes irreversible expansion, akin to visco-plastic flow, with an extensibility (effective viscosity) Φ^w (Fig. 2A). Water flux from extracellular space is proportional to $L^a\Delta\Psi$, where $\Delta\Psi = \Delta\Pi - P$ is the cross-membrane water potential difference (external pressure is assumed to be zero; for the sake of simplicity we set $\Delta\Pi$ constant) and L^a is the conductivity. Intercellular water redistribution via plant plasmodesmata (26), animal gap junctions, or cytoplasmic bridges (27, 28) is driven by intercellular differences in turgor pressure P, with a conductivity L^s. We did not prescribe turgor

135 pressure, instead letting it emerge from local mechanical and hydraulic interplays (see
136 Supplementary Materials and Methods for detailed model description).

137 Whereas cell wall extensibility can be more limiting for growth than water conductivity in fast
138 elongating organs (29), we found that most aquaporin (channel protein allowing rapid water
139 flux (30)) isoforms had significantly lower expression in inflorescence than in other fast
140 growing tissues like stem and root (31) (with a reduction up to ~80%). Therefore we considered
141 limitation of growth by cell wall extensibility and by water conductivity on equal footing. We
142 first imposed slower water flux than cell wall extension, and found that, with homogenous
143 effective parameters, we could recover the turgor–neighbour-number anticorrelation in our
144 model, without or with cell divisions to mimic oryzalin-treated or untreated SAM (no division
145 5 simulations, n = 1219 cells, R = -0.87, $p < 10^{-100}$; dividing 8 simulations, n = 3240 cells, R =
146 -0.58, $p < 10^{-100}$) (Fig. 2B-I). This implies that local hydrostatic pressure heterogeneity does not
147 require differential cellular osmotic pressure (21) in a growing tissue, and predicts a topological
148 origin of pressure variability, similar to liquid foams where pressure heterogeneity is due to fast
149 liquid flow and limited gas diffusion rate between bubbles (24). Indeed, water flow in a tissue
150 parallels gas flow between cells in a foam and mechanics of cell walls replaces the rheology of
151 the liquid films.

152 In order to test the robustness of this result, we explored the parameter space of the vertex
153 model. Analytical exploration in a two-cell system (25) had showed that systems dynamics is
154 controlled by two main dimensionless parameters, α^s, which compares intercellular water
155 conductivity to total (intercellular and transmembrane) conductivity, and α^a, which compares
156 the limitation of growth by transmembrane permeability to the combined limitation of growth
157 by cell wall extensibility and transmembrane permeability (expression of these dimensionless
158 parameters are given in the Methods). Accordingly, our first results, obtained with $\alpha^a = 0.1$ and
159 $\alpha^s = 0.1$, denoted water flux-limited growth. We uplifted this limit, consistently with
160 observations in many cell types (29), by increasing α^a from 0.1 to 0.5 and 0.9, where water
161 conductivity equals or is relatively one magnitude higher than wall extensibility (32), and still
162 recovered the turgor–neighbour-number anticorrelation (Fig. 2J), demonstrating that strong flux
163 limitation is not required for pressure heterogeneity. Next, we relaxed the intercellular flux

limitation, by increasing α^s from 0.1 to 0.5 and 0.9, and showed that the anticorrelation is maintained even when intercellular flux is much stronger than osmotic water uptake (Fig. 2J). Shifting cell size checkpoint at division (by either -25% or +50%), which effectively changes average cell surface-to-volume ratio that antagonistically weighs the contribution of flux and wall limitations, also yields steady turgor–neighbour-number anticorrelation (Fig. 2J). Altogether, the parameter space exploration indicates that topology-related pressure heterogeneity is a robust outcome of the model.

In SAM surface, cell neighbour number and size are coupled (Fig. S9). Consistently, cell-specific turgor pressure anticorrelates with normalized cell area (Fig. S9). To uncouple cell size and topology, we modified the initial state of our simulation to have four-neighboured cells bigger than eight-neighboured cells, and found that higher turgor pressure accumulated in four-neighboured cells, not in the smaller cells (Fig. S9), confirming that turgor pressure heterogeneity emerges from tissue topology rather than cell size differences. This can be explained by local topology, which determines cell wall angles and the subsequent tension distribution at each three-cell junction (Fig. 2K-N): in our model, wall stress and strain above the growth threshold are relaxed at a rate limited by wall extensibility and hydraulic conductivity. Therefore, stress and strain remain close to their values at growth threshold and are almost homogeneous in oryzalin-like simulations (Fig. 2C), and the sum of wall tension at each three-cell junction (vertex) mostly depends on the angles between walls. The vertex between three hexagonal cells with 120° internal angles has a sum of tension at zero (Fig. 2K, L). Fewer-neighboured cells have sharper internal angles, so the sum of tension at vertex is greater towards the cell interior, creating additional inward compression and prompting higher pressure build-up at equilibrium (Fig. 2M, N). In dividing simulations, as in the untreated case, new walls do not bear stress right after division because they form from cell interior. These new walls are gradually strained due to mesh growth but do not yield (expand) to release stress before reaching the threshold (Fig. 2G). Consequently, cell division keeps the wall stress from homogenizing and dampens the turgor–neighbour-number anticorrelation (Fig. 2I). Notably, although tissue topology is sufficient to explain pressure heterogeneity, we do not exclude a role of other biological parameters and/or sources of noise in pressure variations, as suggested

193 by weaker correlations in experiments (Fig. 1F, J) than in simulations. Nonetheless, since tissue
194 topology is highly conserved in many biological systems (33), we propose that hydrostatic
195 pressure heterogeneity may emerge in compact tissues with polygonal cells (34) and non-
196 instantaneous water movement, due to the adjustment to reconcile local mechanical and
197 hydraulic conditions.

198 **Heterogeneity in growth rate is patterned according to the balance between wall**
199 **extensibility and tissue conductivity**

200 Next, we monitored areal growth rate of SAM epidermal cells by time-lapse confocal
201 microscopy. As observed previously, untreated SAMs exhibited slower growth in the central
202 zone (CZ), where stem cells reside, than in the surrounding peripheral zone (PZ) (35) (Fig. S7).
203 In addition, cellular growth rate anticorrelates with neighbour number (11 SAMs, n = 1491
204 cells, R = -0.15, $p = 10^{-8}$; Fig. 3E) and cell size (Fig. 3F; R = -0.33, $p = 10^{-38}$), supporting
205 previous reports that smaller cells in SAM grow faster (36, 37), and suggests that higher turgor
206 pressure in fewer-neighboured cells associates with faster growth. In oryzalin-treated SAMs,
207 however, the fewer-neighboured and small cells grew slower (14 SAMs, n = 1160 cells; Fig.
208 3K, neighbour number R = 0.20, $p = 10^{-11}$; Fig. 3L, cell size R = 0.16, $p = 10^{-8}$). This suggests
209 that higher turgor pressure associates with either faster or slower growth depending on
210 conditions (Fig. S9). Although seemingly a small shift, this negative-to-positive slope change
211 of local growth heterogeneity captures a strong qualitative inversion of growth behaviour (Fig.
212 3D, J), where relative cell size increases exponentially in opposite fashions (Fig. S10).
213 Accordingly, smaller cells expand more than larger cells in untreated SAMs, which may
214 contribute to cell size homeostasis, a phenomenon that would be absent in oryzalin-treated
215 SAMs.

216 We further explored the growth trend in our vertex model. Based on the parameter exploration
217 on dividing mesh aimed to reproduce untreated SAM behaviour, we found both positive and
218 negative correlations between growth rate and cell neighbour number (Fig. S11). This indicates
219 that growth trend is sensitive to parameters that alter the balance between water flux and wall
220 expansion. Conservatively, we chose equal contribution by flux and wall in our model (α^a =
221 0.5), which required scaling up theoretical cell size (by +50%) to maintain growth trend as in

222 untreated SAM: Figures 4A-C show that the fewer-neighboured and smaller cells grow faster
223 (10 simulations, $n = 5971$; G vs N, $R = -0.25$, $p = 10^{-84}$; G vs A, $R = -0.96$, $p < 10^{-100}$).

224 We then attempted to reproduce oryzalin-treated behaviour, guided by the experimental
225 observations that, besides stopping cell division, oryzalin treatment also yields higher osmotic
226 pressure (1.6-fold) and drastically thicker cell walls (4-fold) (Fig. S5, S12). We found that both
227 stalling division and increasing osmotic pressure failed to invert the growth trend in the model,
228 while doubling and quadrupling wall thickness inverted the correlation of growth rate to
229 neighbour number and cell size (Fig. 4D-F, G; S13), like in oryzalin-treated SAM. Combining
230 higher osmotic pressure and thicker wall revealed that quadrupling wall thickness can robustly
231 trigger growth trend inversion (Fig. 4 and Fig. S13).

232 Effectively, changing osmotic pressure and wall thickness also alters the wall–flux limitation
233 balance of the system (Fig. 4G). Higher osmotic pressure induces faster water influx (reduced
234 limitation by flux). The extra volume strains the walls to accumulate stress farther beyond the
235 threshold, which is relaxed by wall yielding (growth) with extensibility as the rate limit.
236 Meanwhile, wall thickening reduces wall stress and strain towards the threshold for expansion,
237 effectively reducing the mechanical drive of growth and increasing the weight of water
238 permeability in limiting growth, similar to liquid foam. We do not exclude other possible
239 parameter changes triggered by oryzalin treatment, like water conductivity and wall synthesis
240 rate, that also contribute to the wall–flux limitation balance. Nevertheless, implementing the
241 observed cell wall thickening in the model is sufficient to explain the observed growth rate
242 inversion from untreated to oryzalin-treated scenario.

243 **Conclusions**

244 In this study, we analysed the intercellular heterogeneity of turgor pressure and its effect on cell
245 growth rate in the epidermis of Arabidopsis SAM, utilizing both indentation experiments and
246 mechanical modelling. We propose that tissue mechanics and hydraulics act in parallel with the
247 established genetic regulations in SAM cell growth. We demonstrate that cellular hydrostatic
248 pressure is innately heterogeneous in Arabidopsis SAM epidermis; however, it is not a proxy
249 of local growth rate variability, contrary to expectations. Instead, our analysis suggests that

250 turgor pressure and growth rate are combinatorial outputs of local mechanics and hydraulics.
251 Each of these parameters can be controlled by genetic and biochemical inputs, and small
252 uniform changes in these biological inputs can enable drastic shifts of cell size distribution (Fig.
253 S14), unlike liquid foams in which cell size distribution always enlarge over time. Our
254 simulation and experiment data suggest that Arabidopsis SAM is likely close to the tipping
255 point between the limits of wall synthesis and water influx. Such inversion in growth trend is
256 not irrelevant to normal development: for example, a growth variability switch is observed
257 during sepal development, where clones of smaller and often fewer-neighboured cells grow
258 faster in young sepals then slower in older sepals, effectively switching from homogenizing to
259 amplifying cell size variability (38). The emergent heterogeneity of local growth and
260 hydrostatic pressure likely underlies morphogenesis in other compact tissues with polygonal
261 cells.

262 **Materials and Methods**

263 **Plant materials, treatments and growth conditions**

264 *Arabidopsis thaliana GFP-LTi6b* (ecotype WS-4) reporter line and ecotype Col-0 was used(39).
265 Untreated inflorescence meristems were obtained from soil-grown plants, first in short-day (8
266 h light 20°C / 16 h dark 19°C cycle) for 3 to 4 weeks then transferred to long-day (16 h light
267 20°C / 8 h dark 19°C cycle) for 1 to 2 weeks to synchronize bolting. Oryzalin-treated
268 inflorescence meristems were obtained from plants grown on custom-made Arabidopsis
269 medium (40) (Duchefa) supplemented with 1% agar-agar (Merck) and 10 µM N-1-
270 naphthylphthalamic acid (NPA, Sigma-Aldrich/Merck) for 3 weeks. Pin-formed inflorescence
271 meristems from NPA medium were immersed in 10 µg/mL oryzalin (Sigma-Aldrich/Merck)
272 twice (3 h duration, 24 h interval) (21). For mechanical measurements and time-lapse confocal
273 imaging, meristems were mounted on Arabidopsis apex culture medium (ACM) (40) with 2%
274 agarose and 0.1% plant preservation mixture (PPM, Plant Cell Technology) to prevent
275 contamination, and cultivated in long-day condition.

276 **Atomic force microscopy and force curve analysis**

277 AFM measurement and analysis were performed as in Beauzamy et al., 2015 (18) with

278 modifications. For detail, see Supplementary Materials and Methods.

279 **Time-lapse confocal microscopy and image processing**

280 Untreated (dissected) and oryzalin-treated meristems were mounted and grown on ACM with
281 0.8% agarose and 0.1% PPM for live imaging. Confocal stacks were taken on an LSM 700
282 confocal microscope (Carl Zeiss) operated with the ZEN 2010 software (version 6.0, Carl
283 Zeiss), using a W N-Achroplan 40x/0.75 M27 water immersion objective, and on a TCS SP8
284 confocal microscope (Leica) operated with the Leica Application Suite X software (version 3.5,
285 Leica), using a Fluotar VISIR 25x/0.95 water immersion lens. GFP was excited at 488 nm and
286 emission detected between 415 – 735 nm. Stacks have resolution of 1028×1028 pixels, with
287 resolution ranging between 3.2 to 4.4 pixels/µm; Z steps were between 0.5 and 0.85µm.

288 For hyperosmotic treatments, meristems were mounted in Petri-dishes on Patafix (UHU), then
289 submerged in liquid ACM containing 0.1% PPM. Samples were first imaged in liquid ACM
290 (plus 0.1% PPM), then submersion medium was changed to ACM plus desired concentration
291 of NaCl (plus 0.1% PPM) by first rinsing with 3~5 mL target solution, then soaked in target
292 solution for 5 minutes before imaging. Because of the reduced signal in hyperosmotic solutions,
293 possibly due to the altered refractive index, stronger gain was used to reach comparable signal
294 intensity.

295 Confocal image stacks were analysed with MorphoGraphX (MGX version 1.0) (41). For details,
296 see Supplementary Materials and Methods.

297 **Statistical analysis**

298 Data were processed using Excel 2000 (Microsoft). All Tukey box plots depict the first, second
299 (median) and third quartiles of data distribution, with whiskers marking the lowest/highest data
300 within 1.5 interquartile ranges (IQR) of the lower/upper quartiles. Tukey's outliers are depicted
301 as small circles outside the whiskers. Values like turgor pressure, cell area and growth rate were
302 normalized to the average per meristem. After normalization, every cell was considered as one
303 biological sample, and all linear regressions and Pearson correlations were performed on whole
304 datasets. For simulations, cells on the edge of the mesh were not analysed due to border effect.
305 Extremely rare polygon classes (i.e. triangle and nonagon) were not shown on the box plots in

306 the main figures but were included in linear regression and Pearson correlation tests and were
307 plotted in Extended data Figure 6. Kolmogorov–Smirnov test was used to distinguish cell
308 neighbour number distribution (significance level $\alpha = 0.01$).

309 **Modelling and FEM simulation**

310 We build a vertex-based model of plant tissues at cellular level that couples osmosis-driven
311 hydraulic fluxes between cells and from apoplast with a fixed water potential, and cell wall
312 mechanics which resists and grows under tension, based on the modelling framework from
313 Cheddadi et al. 2019 (25). Realistic meshes for FEM indentation simulations were generated
314 from confocal stacks, while inflation and indentation simulations were performed with the same
315 procedure adopted from Mosca et al., 2017 (20). For details, see Supplementary Materials and
316 Methods.

317 **Acknowledgements**

318 We thank P. Bolland and A. Lacroix for plant care, G. Cloarec for help with TEM, L. Beauzamy
319 for AFM training, C. Mollier for help in estimating confocal technical errors, A. Kiss for help
320 with anisotropic filtering parameterization, G. Cerrutti for help in implementing the division
321 algorithm and in segmentation and mesh generation for the indentation simulations, and R.
322 Smith for help in segmentation and mesh generation for the indentation simulations. We
323 acknowledge the contribution of the PLATIM facility of SFR Biosciences (UMS3444/CNRS,
324 US8/Inserm, ENS de Lyon, UCBL) for AFM and confocal microscopy, and of Centre
325 Technologique des Microstructures (UCBL, Lyon) for electron microscopy. This work was
326 supported by a fellowship from Institut Universitaire de France and an ERC Starting Grant
327 "PhyMorph" to A.B. (ERC-2012-StG-307387), an EMBO Long-term Fellowship to Y.L.
328 (EMBO ALTF 168-2015), and an Agropolis Foundation grant (MecaFruit3D) to I.C. and C.G.

329 **Author contributions**

330 This study was initiated by A.B. Y.L. and A.B. designed the experiments. Y.L. executed AFM
331 and confocal microscopy, acquired experimental data except EM, and analysed experimental
332 and simulation data. J.T. performed electron microscopy. V.M and M.D. wrote scripts to

facilitate experimental data analysis. I.C. and C.G. designed physical model of tissue growth. I.C. implemented the model, ran simulations, optimized model parameters and analysed simulation data. G.M. designed, ran, and analysed indentation simulations. Y.L. and A.B. contributed to the design of simulations. Y.L., I.C., V.M., G.M., C.G. and A.B. contributed to data interpretation. Y.L. and A.B. wrote the manuscript with inputs from the other authors.

Data availability

All materials, scripts and datasets generated and analysed during the current study are available from the corresponding authors upon reasonable request.

342 **Figures**

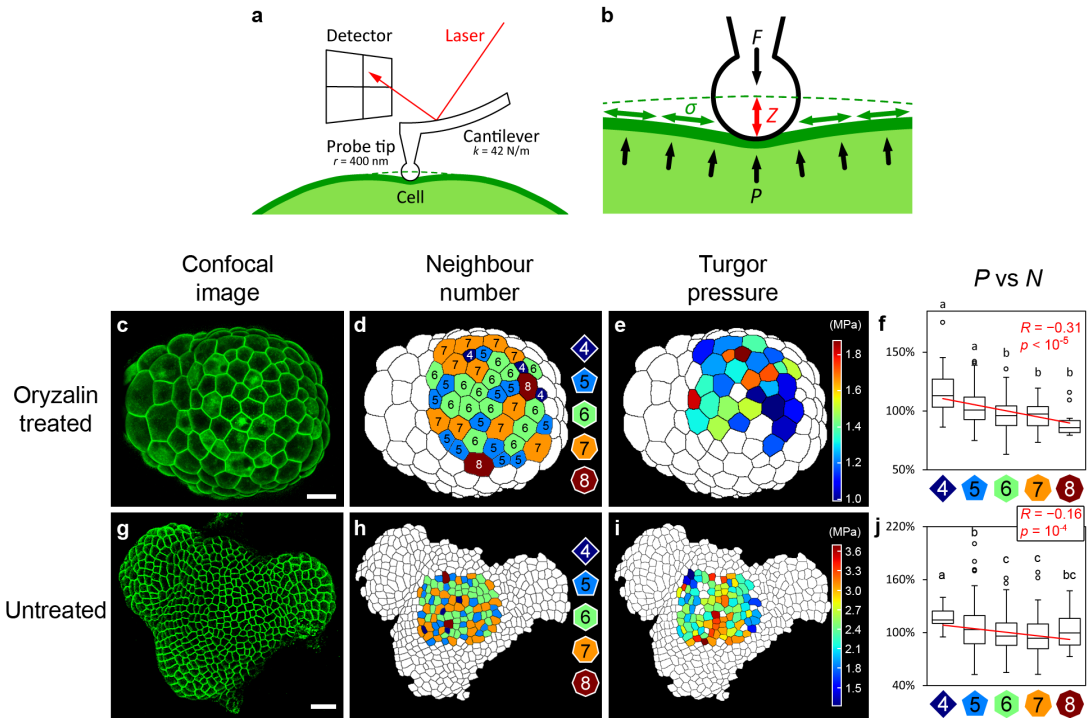

Figure 1. Turgor pressure heterogeneity in SAM is associated with variation of cell topology.

(**a** and **b**) Schematic representation of AFM nanoindentation for turgor pressure measurement. *r*, probe tip radius; *k*, cantilever stiffness; *F*, indentation force; *Z*, indentation depth; *P*, turgor pressure; *σ*, cell wall tension. (**c** to **j**) Cell-specific turgor pressure in oryzalin-treated (c to f) and untreated SAM (g to j). (c and g) Top-view surface projections of SAM, oryzalin-treated (c) or untreated (g), with plasma membrane GFP signal; scale bars represent 20 µm. (d and h) Cell topology determined on segmented cell contour images, around SAM centre; numbers indicate neighbour number in epidermis. (e and i) AFM-determined cell-specific turgor pressure heat maps. (f and j) Box plots of cellular turgor pressure *P* normalized per SAM against cell topology *N* (f, oryzalin-treated 9 SAMs, $n = 202$ cells; j, untreated 7 SAMs, $n = 503$ cells). Circles are Tukey's outliers; lowercase letters indicate statistically different populations (Student's *t*-test, $p < 0.05$); red lines indicate linear regressions, with Pearson correlation coefficient *R* and corresponding *p*-value.

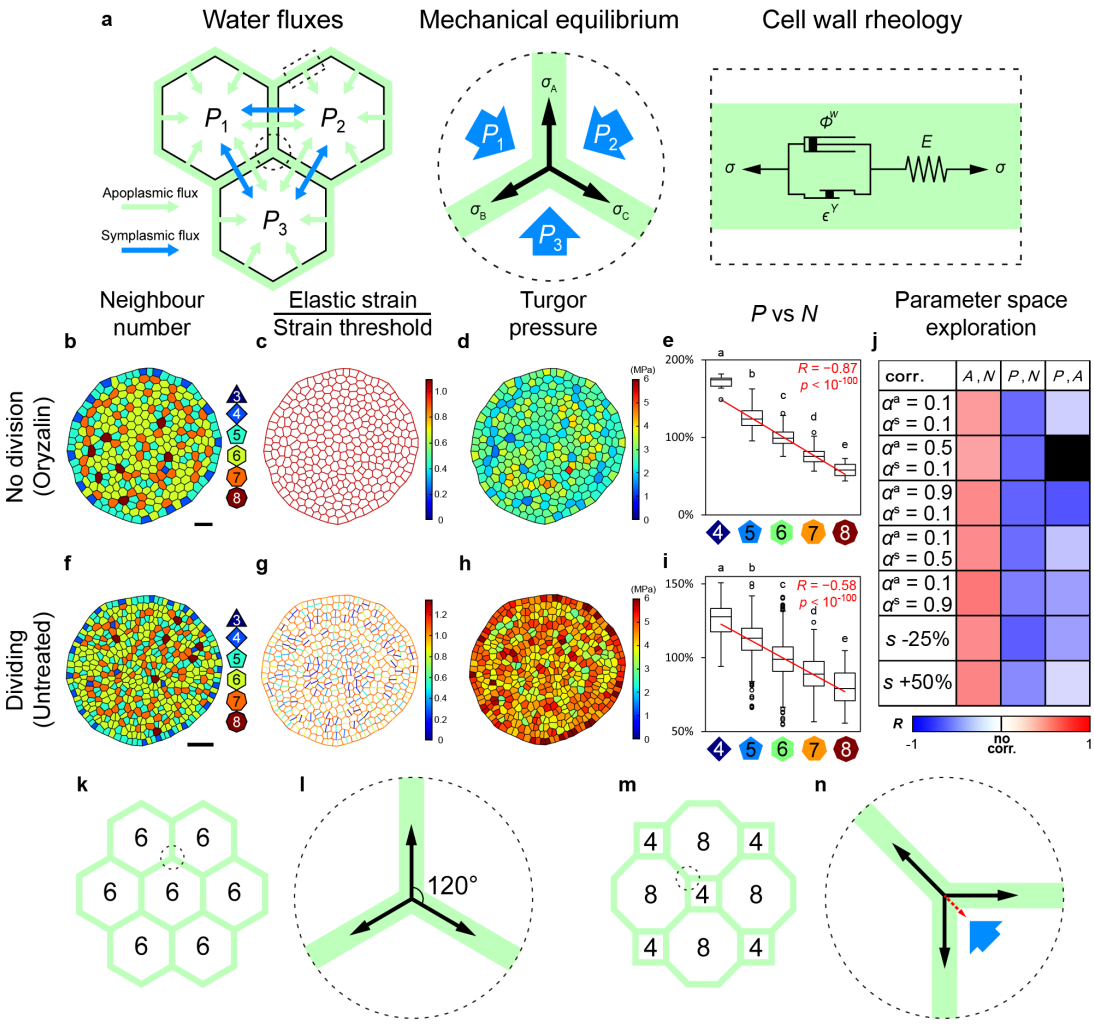

Figure 2. Turgor pressure heterogeneity emerges from cell topology.
(**a**) Schematic representations of model components, including apoplasmic and intercellular water fluxes (left), mechanical equilibrium at three-cell junctions (middle) and the visco-elasto-plastic cell wall rheology. P, cell-specific turgor pressure; σ, cell wall tension; Φ^w, wall extensibility; ϵ^Y, wall strain threshold; E, wall Young's modulus. (**b** to **i**) Turgor pressure in non-dividing (oryzalin-treated, b to e) and dividing (untreated) simulations (f to i), scale bars are 5 unit length. (b and f) Cell topology; (c and g) cell wall strain relative to strain threshold; (d and h) cellular turgor pressure heat maps; (e and i) Box plots of normalized cellular turgor pressure P against cell topology N (d, non-dividing 5 simulations, $n = 1219$ cells; g, dividing 8 simulations, $n = 3240$ cells). Cells on the mesh edge were not analysed due to border effect. Circles are Tukey's outliers; lowercase letters indicate statistically different populations (Student's t-test, $p < 0.05$); red lines indicate linear regressions, with Pearson correlation coefficient R and corresponding p-value. (**j**) Model parameter exploration. Colours indicate Person correlation R, with perfect anticorrelation as blue ($R = -1$), perfect correlation in red ($R = 1$), and insignificant correlation ($p > 0.05$) in black. A, normalized cell area; N, cell neighbour number; P, normalized turgor pressure; α^a, dimensionless parameter for flux-wall limit balance; α^s, dimensionless parameter for apoplasmic-symplasmic limit balance; s, cell size at division (**k** to **n**) Schematic explanation of topology-derived turgor pressure heterogeneity. (k and l) Three-cell junctions in a tissue of hexagonal cells are at mechanical

equilibrium with equal tensions and equal wall-wall angles. (m and n) Fewer-neighboured cells have sharper wall-wall angles, a tension that is roughly constant per wall effectively results in mechanical compression due to unequal projected tension distribution (red dash-line arrow) that is balanced by higher turgor pressure build-up (big blue arrow).

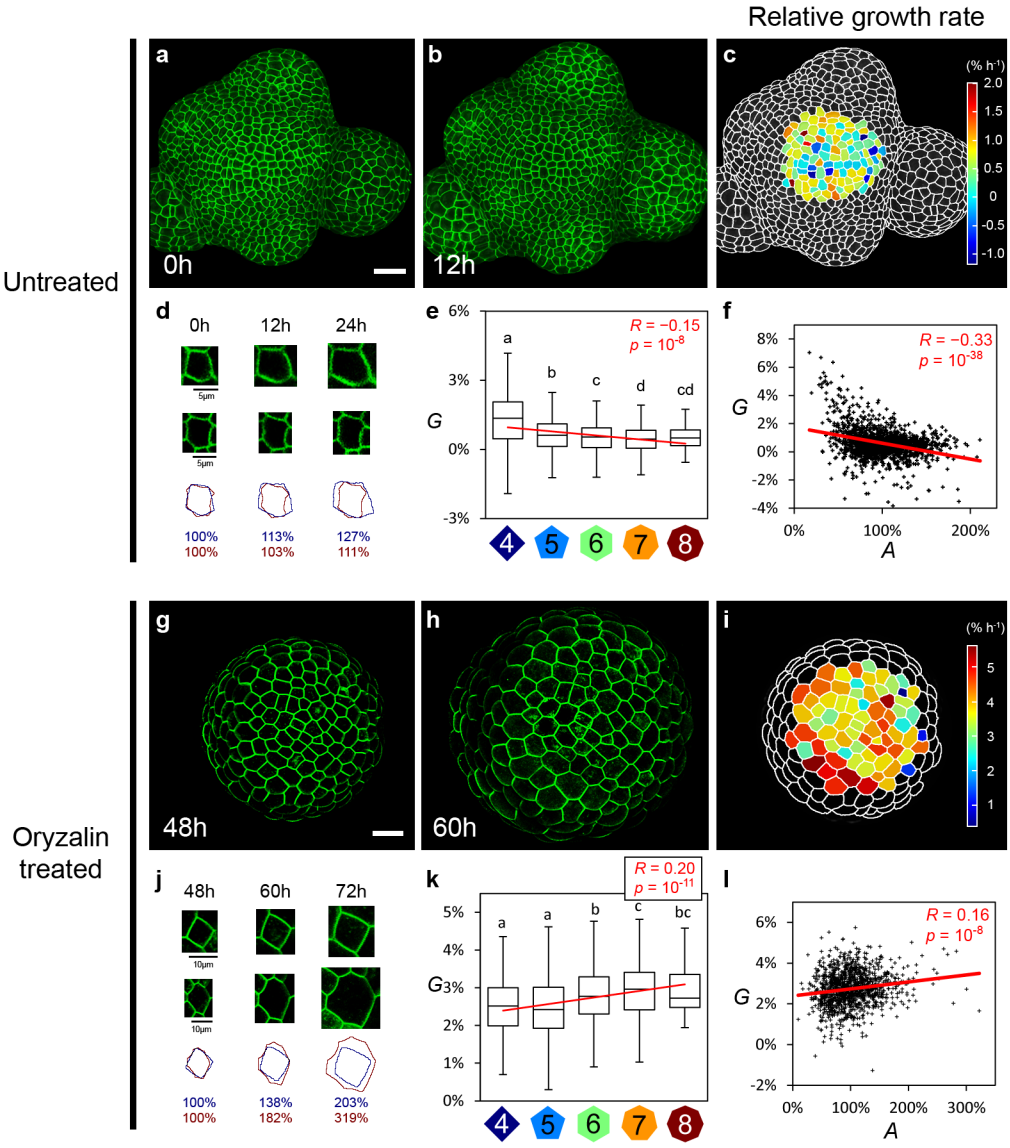

Figure 3. Cellular growth rate bifurcates between conditions.
(**a** to **f**) Relative growth rate per hour *G* of untreated SAM cells between 12-hour interval. (**g** to **l**) Cellular growth rate per hour of oryzalin-treated SAM between 12-hour interval (48 and 60 hours post treatment). (a, b, g and h) Surface projections of untreated or oryzalin-treated SAM at initial time point (a and g) and 12 hours later (b and h); scale bars are 20 µm unless otherwise noted. (c and i) Heat maps of areal relative growth rate per hour. (d and j) Example 4 and 8-neighbored cells during 24-hour growth, with areal normalization at initial time point. Cell contour and relative size (blue for 4-neighbored, red for 8-neighbored) depict the diverging growth trends. Scale bars are as indicated. (e, f, k and l) Box plots of relative growth rate per hour *G* against cell topology *N* (e and k) and dot plots of relative growth rate per hour *G* against normalized cell area *A* (f and l) (e and f, untreated 11 SAMs, n = 1491 cells;

k and l, oryzalin-treated 14 SAMs, $n = 1160$ cells). Note that Tukey's outliers are not plotted, but are included for statistical analyses. Lowercase letters indicate statistically different populations (Student's t-test, $p < 0.05$); red lines indicate linear regressions, with Pearson correlation coefficient R and corresponding p-value.

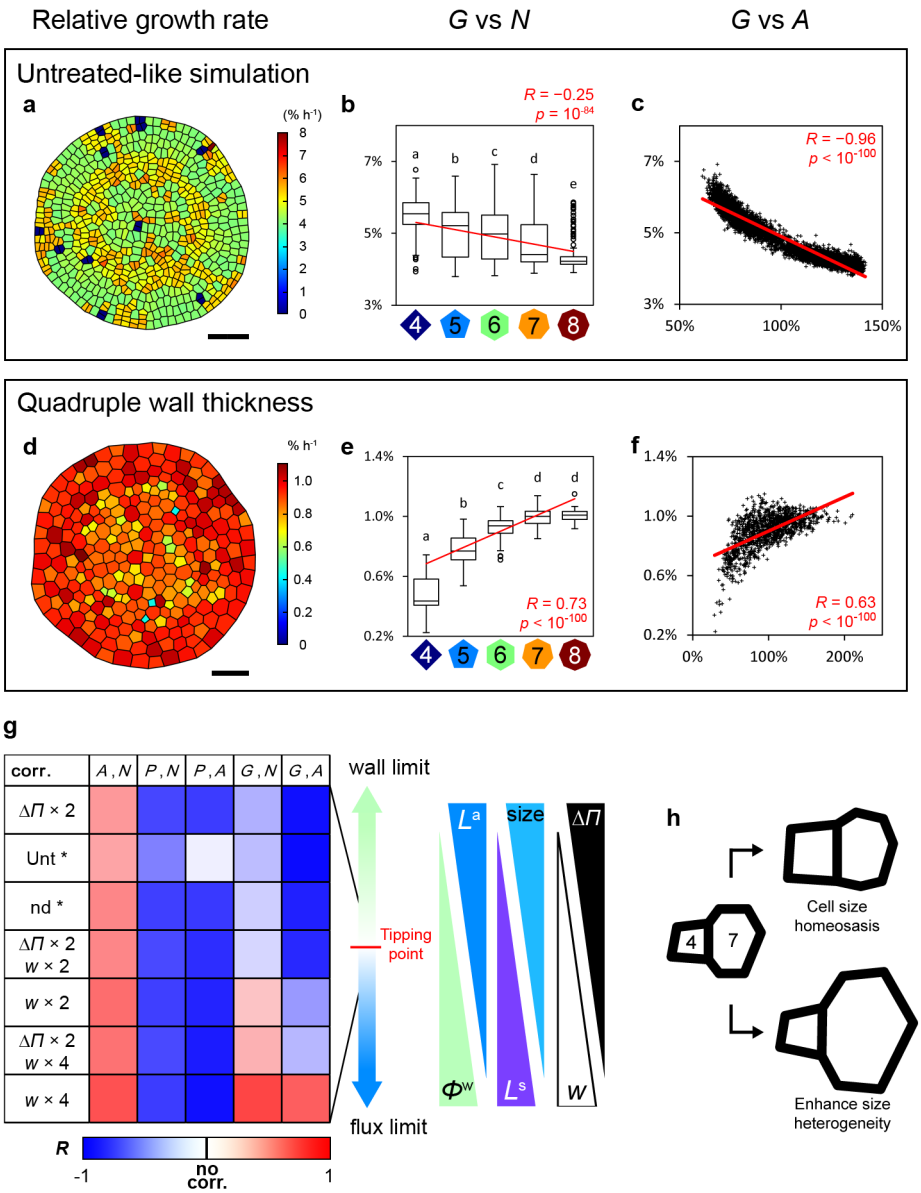

Figure 4. Model effective parameters that enable recapitulating the untreated and oryzalin-treated growth trends.

(**a** to **c**) Relative growth rate per hour G in simulations with cell division, which corresponds to $\alpha^a = 0.5$ and division size s +50%, and mimics untreated SAM. Cells that just divided (dark blue with 0 growth) are not included in analysis. (**d** to **f**) Growth simulations with no cell division, $\alpha^a = 0.5$, and quadruple wall thickness to mimic oryzalin treatment. (a, d) Heat maps of areal relative growth rate per hour. Scale bars are 10 unit lengths. (b, e) Box plots of relative growth rate per hour G against cell topology N. Lowercase letters indicate statistically different populations (Student's t-test, $p < 0.05$); red lines indicate linear regressions, with Pearson correlation coefficient R and corresponding p-value. (c, f) Dot plots

of relative growth rate per hour G against normalized cell area A. Numbers of repeats see Methods. (**g**) Model exploration to fit oryzalin-treated case. Colours indicate Person correlation R, with perfect anticorrelation as blue (R = -1), perfect correlation in red (R = 1), and insignificant correlation ($p > 0.05$) in black. Triangles indicate parameter's influence to the flux-wall limit balance. * indicates the same parameter choices ($\alpha^a = 0.5$ and division size s +50%), with Unt indicating dividing, untreated-like simulations and nd for non-dividing; $\Delta\Pi$, osmotic drive; w, wall thickness; A, normalized cell area; N, cell neighbour number; P, normalized turgor pressure; G, relative growth rate; Φ^w, wall extensibility; L^a, cross-membrane water conductivity; L^s, cell-to-cell symplasmic conductivity; size, cell size at division. (**h**) Summary of growth trend inversion according to the flux-wall limits shown in (g).

343

344 **References**

345 1. Hong L, et al. (2018) Heterogeneity and Robustness in Plant Morphogenesis: From Cells to
346 Organs. *Annu Rev Plant Biol* 69(1):469–495.

347 2. Kamimoto K, et al. (2016) Heterogeneity and stochastic growth regulation of biliary epithelial
348 cells dictate dynamic epithelial tissue remodeling. *eLife* 5. doi:10.7554/eLife.15034.

349 3. Ietswaart R, Rosa S, Wu Z, Dean C, Howard M (2017) Cell-Size-Dependent Transcription of
350 FLC and Its Antisense Long Non-coding RNA COOLAIR Explain Cell-to-Cell Expression Variation.
351 *Cell Syst* 4(6):622-635.e9.

352 4. Long Y, et al. (2017) In vivo FRET-FLIM reveals cell-type-specific protein interactions in
353 Arabidopsis roots. *Nature* 548(7665):97–102.

354 5. Chubb JR (2017) Symmetry breaking in development and stochastic gene expression. *Wiley*
355 *Interdiscip Rev Dev Biol* 6(6):e284.

356 6. Donati G, Watt FM (2015) Stem Cell Heterogeneity and Plasticity in Epithelia. *Cell Stem Cell*
357 16(5):465–476.

358 7. Gerdes MJ, et al. (2014) Emerging Understanding of Multiscale Tumor Heterogeneity. *Front*
359 *Oncol* 4. doi:10.3389/fonc.2014.00366.

360 8. Eldar A, Elowitz MB (2010) Functional roles for noise in genetic circuits. *Nature*
361 467(7312):167–173.

362 9. Watanabe K, Umeda T, Niwa K, Naguro I, Ichijo H (2018) A PP6-ASK3 Module Coordinates the
363 Bidirectional Cell Volume Regulation under Osmotic Stress. *Cell Rep* 22(11):2809–2817.

364 10. Xie K, Yang Y, Jiang H (2018) Controlling Cellular Volume via Mechanical and Physical
365 Properties of Substrate. *Biophys J* 114(3):675–687.

366 11. Guo M, et al. (2017) Cell volume change through water efflux impacts cell stiffness and stem
367 cell fate. *Proc Natl Acad Sci* 114(41):E8618–E8627.

368 12. Dumais J, Forterre Y (2012) "Vegetable Dynamicks": The Role of Water in Plant Movements.
369 *Annu Rev Fluid Mech* 44(1):453–478.

370 13. Stewart MP, et al. (2011) Hydrostatic pressure and the actomyosin cortex drive mitotic cell
371 rounding. *Nature* 469(7329):226–230.

372 14. Montel F, et al. (2011) Stress clamp experiments on multicellular tumor spheroids. *Phys Rev*
373 *Lett* 107(18):188102.

374 15. Rojas ER, Huang KC (2017) Regulation of microbial growth by turgor pressure. *Curr Opin*
375 *Microbiol* 42:62–70.

376 16. Kroeger JH, Zerzour R, Geitmann A (2011) Regulator or driving force? The role of turgor
377 pressure in oscillatory plant cell growth. *PloS One* 6(4):e18549.

378 17. Ortega JK (1985) Augmented growth equation for cell wall expansion. *Plant Physiol*
379 79(1):318–320.

380 18. Beauzamy L, Derr J, Boudaoud A (2015) Quantifying Hydrostatic Pressure in Plant Cells by
381 Using Indentation with an Atomic Force Microscope. *Biophys J* 108(10):2448–2456.

382 19. Vella D, Ajdari A, Vaziri A, Boudaoud A (2012) The indentation of pressurized elastic shells:
383 from polymeric capsules to yeast cells. *J R Soc Interface* 9(68):448–455.

384 20. Mosca G, Sapala A, Strauss S, Routier-Kierzkowska A-L, Smith RS (2017) On the micro-
385 indentation of plant cells in a tissue context. *Phys Biol* 14(1):015003.

386 21. Corson F, et al. (2009) Turning a plant tissue into a living cell froth through isotropic growth.
387 *Proc Natl Acad Sci U S A* 106(21):8453–8458.

388 22. Beauzamy L, Louveaux M, Hamant O, Boudaoud A (2015) Mechanically, the Shoot Apical
389 Meristem of Arabidopsis Behaves like a Shell Inflated by a Pressure of About 1 MPa. *Front*
390 *Plant Sci* 6. doi:10.3389/fpls.2015.01038.

391 23. Ishihara S, et al. (2013) Comparative study of non-invasive force and stress inference
392 methods in tissue. *Eur Phys J E Soft Matter* 36(4):9859.

393 24. Weaire DL, Hutzler S (2001) *The Physics of Foams* (Clarendon Press).

394 25. Cheddadi I, Génard M, Bertin N, Godin C (2019) Coupling water fluxes with cell wall
395 mechanics in a multicellular model of plant development. *PLOS Comput Biol* 15(6):e1007121.

396 26. Lucas WJ, Ham B-K, Kim J-Y (2009) Plasmodesmata - bridging the gap between neighboring
397 plant cells. *Trends Cell Biol* 19(10):495–503.

398 27. Kumar NM, Gilula NB (1996) The Gap Junction Communication Channel. *Cell* 84(3):381–388.

399 28. McLean PF, Cooley L (2013) Protein Equilibration through Somatic Ring Canals in Drosophila.
400 *Science* 340(6139). doi:10.1126/science.1234887.

401 29. Cosgrove DJ (1993) Wall extensibility: its nature, measurement and relationship to plant
402 cell growth. *New Phytol* 124(1):1–23.

403 30. Maurel C, et al. (2015) Aquaporins in Plants. *Physiol Rev* 95(4):1321–1358.

404 31. Klepikova AV, Kasianov AS, Gerasimov ES, Logacheva MD, Penin AA (2016) A high resolution
405 map of the Arabidopsis thaliana developmental transcriptome based on RNA-seq profiling.
406 *Plant J Cell Mol Biol* 88(6):1058–1070.

407 32. Ortega JKE (2019) Dimensionless Numbers to Analyze Expansive Growth Processes. *Plants*

408 8(1):17.

409 33. Gibson WT, Gibson MC (2009) Chapter 4 Cell Topology, Geometry, and Morphogenesis in
410 Proliferating Epithelia. *Current Topics in Developmental Biology*, Current Topics in
411 Developmental Biology. (Academic Press), pp 87–114.

412 34. Péret B, et al. (2012) Auxin regulates aquaporin function to facilitate lateral root emergence.
413 *Nat Cell Biol* 14(10):991–998.

414 35. Kwiatkowska D (2004) Surface growth at the reproductive shoot apex of Arabidopsis thaliana
415 pin-formed 1 and wild type. *J Exp Bot* 55(399):1021–1032.

416 36. Serrano-Mislata A, Schiessl K, Sablowski R (2015) Active Control of Cell Size Generates Spatial
417 Detail during Plant Organogenesis. *Curr Biol* 25(22):2991–2996.

418 37. Willis L, et al. (2016) Cell size and growth regulation in the Arabidopsis thaliana apical stem
419 cell niche. *Proc Natl Acad Sci U S A* 113(51):E8238–E8246.

420 38. Tsugawa S, et al. (2017) Clones of cells switch from reduction to enhancement of size
421 variability in Arabidopsis sepals. *Development* 144(23):4398–4405.

422 39. Cutler SR, Ehrhardt DW, Griffitts JS, Somerville CR (2000) Random GFP∶∶cDNA fusions enable
423 visualization of subcellular structures in cells of Arabidopsis at a high frequency. *Proc Natl*
424 *Acad Sci* 97(7):3718–3723.

425 40. Stanislas T, Hamant O, Traas J (2017) Chapter 11 - In-vivo analysis of morphogenesis in plants.
426 *Methods in Cell Biology*, Cell Polarity and Morphogenesis., ed Lecuit T (Academic Press), pp
427 203–223.

428 41. Reuille PB de, et al. (2015) MorphoGraphX: A platform for quantifying morphogenesis in 4D.
429 *eLife* 4:e05864.

430